

Thesis Title

A subtitle of your thesis

Author name



Thesis submitted for the degree of
Master in Master's Program Name <change at
main.tex>
60 credits

Department Name <change at main.tex>
Faculty name <change in duoforside.tex>

UNIVERSITY OF OSLO

Spring 2022

Thesis Title

A subtitle of your thesis

Author name

© 2022 Author name

Thesis Title

<http://www.duo.uio.no/>

Printed: Reprosentralen, University of Oslo

Abstract

Contents

1	Introduction	1
I	Theory	3
2	High-Entropy alloys	4
2.1	Fundamentals	4
2.2	Core effects and properties	7
3	Modeling of random alloys	9
3.1	The Special Quasi-random Structure model	9
3.1.1	Mathematical description	10
3.1.2	Applications to high-entropy alloys	12
4	Density Functional Theory	16
4.1	Review of Quantum Mechanics	17
4.1.1	The Shrödinger equation	17
4.1.2	Approximations to the many-body Shrödinger equation	18
4.2	Kohn-Sham density functional theory	20
4.2.1	Density functional theory	20
4.2.2	The Kohn-Sham Equation	21
4.3	Limitations of DFT	22
II	Method	24
5	Practical aspects of DFT	25
5.1	The Exchange-Correlation functional	25
5.1.1	Local density approximation	25
5.1.2	Generalized gradient approximation	26
5.1.3	Meta-GGA	26
5.1.4	Hybrid functionals	27
5.1.5	Outlook	27
5.2	Practical aspects	28
5.3	Self-consistent field calculation	30

6	Computational details	32
6.1	Vienna Ab initio Simulation Package	32
6.2	Generation of SQS	34
6.3	Utility scripts	35
III	Results and Discussion	37
7	(CrFeMnNi)Si₂ in the β-FeSi₂ structure	39
7.1	Bulk β -FeSi ₂	39
7.2	(CrFeMnNi)Si ₂ SQSs	40
7.2.1	The band gap	42
7.2.2	Local and projected density of states	45
7.2.3	The band gap with SCAN and HSE06	47
7.2.4	Pair distribution functions	52
7.2.5	SQS size	54
8	Different compositions	58
8.1	Exploring the quaternary phasidiagram	58
8.2	Replacing elements	63
10	Overview and outlook	65
10.1	Literature	65
10.2	General thoughts	66
10.3	Other things	70
10.4	Cr ₄ Fe ₄ Mn ₄ Ni ₄ Si ₃₂ in different crystal structures	73
10.5	Overview	75
IV	Conclusion	76
A	Compositions	73
A.1	Projected density of states	73
A.2	Probability distribution functions	76
B	Eqvimolar alloy	78
B.1	DOS	78
C	Charge density	80

List of Figures

2.1	Formation of HEA based on δ and N . Figures adopted from [hea2016_ch2]	6
2.2	A schematic illustration of lattice distortion in high-entropy alloys. Figure from [owen_jones_2018]	8
3.1	PDFs of (a) 20 and (b) 250 atom SQS models of CrFeMnNi [hea2016_ch10]	13
3.2	Density of states with SQS and MC/MD of FCC CoCrFeNi, figure from [hea2016_ch10]	14
3.3	Probability distribution functions with SQS and MC/MD of HCP CoOsReRu [hea2016_ch10]	14
4.1	Number of DFT studies per year from 1980 to 2021 [dimensions].	16
5.1	Calculated to experimental band gap measurements of Becke-Johnsoon, modified Becke-Johnson and SCAN functionals [10]	27
5.2	Self consistent iteration of a DFT calculation. Figure adopted from lecture notes fys-mena4111 cite	31
6.1	48 atom SQS based on eqvimolar distribution of Cr, Fe, Mn and Ni in and $FeSi_2$ cell.	36
7.1	Density of states (PBE) β - $FeSi_2$	39
7.2	Density of states of SQS D (CrFeMnNi) Si_2 with PBE.	42
7.3	Density of states of SQS B (CrFeMnNi) Si_2 with PBE.	42
7.4	Local density of states of Si (SQS D)	45
7.5	Local density of states of (a) Cr, (b) Mn, (c) Fe, (d) Ni in SQS D.	45
7.6	Projected density of states SQS D CFMN (fesi2) from PBE calculation	46
7.7	Projected density of states of SQS D and B around E_F	46
7.8	Density of states illustrating the band gaps from PBE and SCAN calculations for SQS E and D.	48
7.9	Density of states of SQS B with HSE06	48
7.10	Probability distribution function of SQS D (top) and B (bottom)	52
7.11	CPU time, Make log plot instead	54
7.12	Density of states of SQS E 192 atom SQS.	56

7.13	Pair distribution functions of SQS sizes (top) 48 atoms, (middle) 96 atoms, (bottom) 192 atoms	57
8.1	Projected density of states of (a) $\text{Cr}_3\text{Fe}_3\text{Mn}_7\text{Ni}_3\text{Si}_{32}$ (SQS B), (b) $\text{Cr}_5\text{Fe}_5\text{Mn}_3\text{Ni}_3\text{Si}_{32}$ (SQS C), (c) $\text{Cr}_5\text{Fe}_3\text{Mn}_5\text{Ni}_3\text{Si}_{32}$ (SQS A), (d) $\text{Cr}_3\text{Fe}_5\text{Mn}_5\text{Ni}_3\text{Si}_{32}$ (SQS D)	61
8.2	Projected density of states of $\text{Cr}_3\text{Fe}_3\text{Mn}_3\text{Ni}_7\text{Si}_{32}$ around E_F .	62
8.3	Projected density of states of $(\text{CrFeMnCo})\text{Si}_2$	65
8.4	Density of states of a) $(\text{CrFeCoNi})\text{Si}_2$ and b) $(\text{CrFeTiNi})\text{Si}_2$. .	66
8.5	Density of states of two SQSs of $(\text{CoFeMnNi})\text{Si}_2$	66
A.1	$\text{chCr}_4\text{Fe}_4\text{Co}_4\text{Ni}_4\text{Si}_{32}$	73
A.2	$\text{chCo}_4\text{Fe}_4\text{Mn}_4\text{Ni}_4\text{Si}_{32}$	74
A.3	$\text{chCr}_4\text{Fe}_4\text{Mn}_4\text{Co}_4\text{Si}_{32}$	74
A.4	$\text{chCr}_4\text{Fe}_4\text{Ti}_4\text{Ni}_4\text{Si}_{32}$	75
A.5	$\text{chCr}_4\text{Fe}_4\text{Mn}_4\text{Ti}_4\text{Si}_{32}$	75
A.6	Probability distribution functions of top: $\text{Co}_4\text{Fe}_4\text{Mn}_4\text{Ni}_4\text{Si}_{32}$ (SQS D), middle: $\text{Cr}_4\text{Fe}_4\text{Co}_4\text{Ni}_4\text{Si}_{32}$ (SQS B), bottom: $\text{Cr}_4\text{Fe}_4\text{Mn}_4\text{Co}_4\text{Si}_{32}$ (SQS B)	76
A.7	Probability distribution function of top: $\text{Cr}_4\text{Fe}_4\text{Mn}_4\text{Ti}_4\text{Si}_{32}$ (SQS B), bottom: $\text{Cr}_4\text{Fe}_4\text{Ti}_4\text{Ni}_4\text{Si}_{32}$ (SQS B))	77
B.1	Density of states SQS A $(\text{CrFeMnNi})\text{Si}_2$ with PBE.	78
B.2	Density of states SQS E $(\text{CrFeMnNi})\text{Si}_2$ with PBE.	79

List of Tables

7.1	Total energy per atom, final magnetic moment and band gap of 5 unique SQS of (CrFeMnNi)Si ₂ based on the β -FeSi ₂ unit cell.	40
7.2	Band gap of the 5 SQSs of (CrFeMnNi)Si ₂ calculated from the eigenvalues in spin up, down and total.	43
7.3	Band gap of SQS D as a function of occupancy in the eigenvalues.	44
7.4	Band gap calculated with PBE, SCAN and HSE06 XC-functionals of (CrFeMnNi)Si ₂ SQSs.	47
7.5	Minimum gap between k-point in valence band and conduction band in SQS B from PBE, SCAN and HSE06	49
7.6	Band gap from HSE06 calculations with gaussian smearing and smearing width <i>sigma</i> equal to 0.05 and 0.005, and the tetrahedron method (TBC). "-" mean unchanged values, "ND" means not done.	50
7.7	Overview 48, 96 and 192 SQSs.	54
7.8	Band gap of SQSs of 48, 96 and 192 atoms each of (CrFeMnNi)Si ₂ . The names are arbitrary, ie A in 48 does not equal A in 96 or 192.	55
8.1	Summary composition diagram	58
8.2	Band gaps of various compositions of (CrFeMnNi)Si ₂ . Most stable SQS of a set is highlighted in bold text, defect band gap are listed in cursive. Some SQSs were excluded from the table due to unsuccessful calculations.	60
8.3	Overview new compositions	63
8.4	Final magnetic moment of the most stable supercell of each composition.	64
8.5	Band gaps of the most stable SQS of β -FeSi ₂ high-entropy silicide compositions as a function of occupancy in the eigenvalues.	65
10.1	Mean and standard deviation of the total energy and magnetic moment per atom, plus enthalpy of formation of the listed mean energies (FeSi ₂).	68

10.2 Total and spin dependent band gap of 4 permutations of CFMN (fesi2) with PBE GGA calculation. The structures that are excluded from this list either failed in calculations, or does not show any band gap.<	70
---	----

Preface

Chapter 1

Introduction

some introduction on the importance of discovering new materials and alloying.

Need something on thermoelectricity related to both the band gap and high-entropy alloys.

High-entropy alloys is a novel class of materials based on alloying multiple components, as opposed to the more traditional binary alloys. This results in an unprecedented opportunity for discovery of new materials with a superior degree of tuning for specific properties and applications. Recent research on high-entropy alloys have resulted in materials with exceedingly strong mechanical properties such as strength, corrosion and temperature resistance, etc **find references**. Meanwhile, the functional properties of high-entropy alloys is vastly unexplored. In this study, we attempt to broaden the knowledge of this field, the precise formulation of this thesis would be an exploration on the possibilities of semiconducting high-entropy alloys.

A key motivation of this thesis is the ability to perform such a broad study of complex materials in light of the advances in material informatics and computational methods. In this project, we will employ Ab initio methods backed by density functional theory on top-of the line supercomputers and software. 20 years ago, at the breaking point of these methods, this study would have been significantly narrower and less detailed firstly, but secondly would have totaled ... amount of CPU hours to complete (**Calculate this number**). In the addition to the development in computational power, is also the progress of modeling materials, specifically we will apply a method called Special Quasi-random Structures (SQS) to model high-entropy alloys or generally computationally complex structures. Together with the open landscape of high-entropy alloys described above, these factors produce a relevant study in the direction of applying modern computational methods to progress the research of a novel material class and point to promising directions for future research.

In specifics, this thesis revolve around the electrical properties of high-entropy alloys, mainly the band gap as this is the key indicator for a semiconducting material and it's applicability. Semiconductors are the building blocks in many different applications in today's world, ranging

from optical and electrical devices, to renewable energy sources such as solar and thermoelectricity. Given the economic and sustainable factors concerning silicon, in addition to its role in relevant applications such as microelectronics and solar power. Silicon emerges as a natural selection to build our alloys around. Furthermore, the development and research on both high entropy alloys and metal silicides have been heavily centered around 3d transition metals. Keeping in line with the economic and environmental factors, we will continue this direction by focusing on high entropy stabilized sustainable and economic 3d metal silicides **Not happy with this writing**. Throughout the study we will analyze a great number of permutations of 3d silicides, from different initial metal silicides such as $CrSi_2$, $FeSi_2$, $MnSi_{1.75}$, Fe_2Si , each with distinct properties relating to the band gap, crystal structure and metal to silicon ratio. In addition, the permutations include numerous metal distributions and elements within the 3d-group of metals. Examples are Co, Cr, Fe, Mn, and Ni.

Given a background in high-entropy alloys, one could ask if this study is truly sensible. In the later sections we will cover the details of this field, and it quickly become clear that the materials investigated in this study does not fall under the precise definition of high-entropy alloys, nor do we intend to explore the properties and factors relating to high-entropy stabilized alloys such as the configurational entropy, phase stability and finite temperature studies. However this study is motivated from the discovery of these materials and promising properties, and venture into a more hypothetical space of materials, enabled by the computational methods available to study the potential properties of such materials. On the other hand, very recent studies **Mari, and other HEA silicide study** have experimentally synthesized high-entropy disilicides, thus in some way justifying the direction of this project.

We begin this project by reviewing key concepts of solid-state physics for readers lacking a background in materials science, and an introduction to the base 3d silicides of the experimental work. Later follows a theoretic walk-through of the relevant concepts of this thesis, these topics include high-entropy alloys, special quasi-random structures, and density functional theory. Next we shine light on the implementation of DFT in this project, and other computational details required to reproduce the results in this thesis, such as the use of the Vienna Ab Initio Simulation Package (VASP) and implementation of SQS. Finally we present the results of our study, these include the band gap and electronic properties of various structures and the success and challenges of the computational methods applied throughout the study.

Part I

Theory

Part II

Method

Chapter 5

Practical aspects of DFT

5.1 The Exchange-Correlation functional

From the former section, we know that the one piece of information missing of the density functional theory is the complex exchange-correlation energy $E_{xc}[n]$ that must account for all the simplifications and approximations employed in Kohn-Sham DFT. In this section we will explore some of the commonly used approximations to exchange-correlation functional. In this project we limit ourselves to 4 levels of complexity, first is the local density approximation (LDA), followed by the generalized gradient approximation (GGA). These two are the least complex and computationally affordable methods. Next is the methods such as meta-GGA implementations and finally the very accurate, but equally demanding hybrid-functionals. In addition, we have methods such as DFT+U, the Minnesota functionals, and double hybrids plus more, but these are outside the scope of this project.

5.1.1 Local density approximation

A homogeneous electron gas (HEG) is the sole case we know of where the exchange-correlation functional can be determined exactly, because in this simple case the electron density is constant. The LDA works by setting the exchange-correlation potential $V_{xc}(\mathbf{r})$ at every position equal to that of the homogeneous electron gas, ie

$$V_{xc}(\mathbf{r}) = V_{xc}^{\text{HEG}}[n(\mathbf{r})]. \quad (5.1)$$

Obviously the LDA is of limited use given that a large part of what makes materials interesting is the variation in the electronic density. In the case of limitations LDA is for example known to overestimate binding energies and underestimate the band gap in semiconductors and insulators. On the other hand, LDA provide generally adequate results in bulk materials with slowly varying charge density, for example equilibrium distances and vibrational frequencies. The biggest upside of LDA however comes from the low computational cost, and was one of the first big success-stories of DFT.

5.1.2 Generalized gradient approximation

A natural succession to the local density approximation is the family of generalized gradient approximation (GGA) that also include the gradient of the electron density

$$V_{\text{XC}}^{\text{GGA}}(\mathbf{r}) = V_{\text{XC}}[n(\mathbf{r}), \nabla n(\mathbf{r})]. \quad (5.2)$$

The way one can implement the gradient are plenty-full and complicated. Two of the most common methods are the Perdew-Wang 91 (PW91) [1] and the Perdew-Burke-Ernzerhof (PBE) GGA [2]. This project will utilize the latter, which came to fruition in 1996 in an article by Perdew, Burke and Ernzerhof appropriately named "Generalized Gradient Approximation Made Simple". The key point regarding the PBE functional is that it's a non-empirical method thus providing reliable and adequate accuracy over a wide range of systems, as compared to for instance the BLYP functional that provide excellent accuracy of organic molecules but fails in other cases [3].

5.1.3 Meta-GGA

Meta-GGA functionals is the final level of complexity of the non-empirical approximations to the exchange-correlation functional. In addition to the the constant density (LDA) and local gradient of the density (GGA), meta-GGA methods consider the kinetic energy density of the occupied Kohn-Sham orbitals [4]

$$\tau_{\omega} = \sum_i^{\text{occ}} \frac{1}{2} |\nabla \psi_{i\omega}|^2. \quad (5.3)$$

The role of this quantity on the the calculated band gap is well described in [5]. In this project we employ a meta-GGA functional named *Strongly Constrained Appropriately Normed*, or SCAN. This functional is the only known functional to satisfy all 17 known exact constraints of the XC functional [6]. The SCAN functional have found evidence of particularly superior accuracy of energies and geometries especially in diversly bonded structures [7], and some indication of improved band gaps and density of states over GGA and LDA functionals [8]. However delivers overall less accurate band gaps compared to other meta-GGA functionals such as the *modified Becke-Johnson* [9]. Unfortunately, MBJ proved too difficult to converge for the particular materials in this project and we instead opt for SCAN.

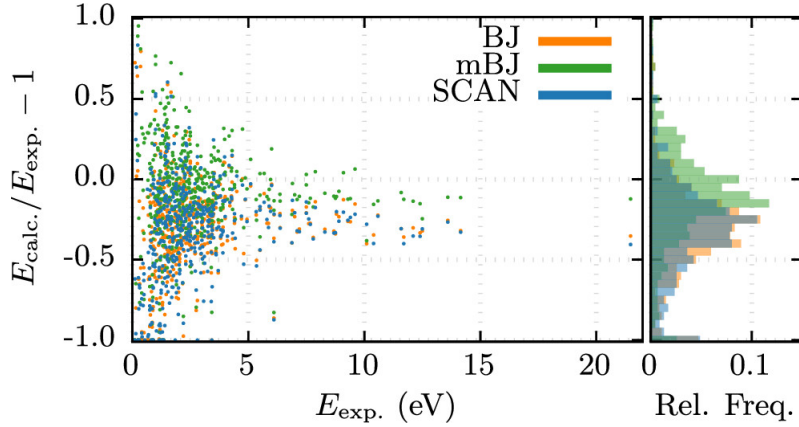


Figure 5.1: Calculated to experimental band gap measurements of Becke-Johnson, modified Becke-Johnson and SCAN functionals [10]

5.1.4 Hybrid functionals

The most accurate functional we employ in this project belong to the family of *hybrid functionals*. Accordingly this method consist of a hybrids between simpler functionals such as LDA, PBE or even meta-GGA and the exact treatment of exchange energy from Hartree-Fock, for example the global hybrid functional PBE0 [11] described as

$$E_{xc}^{PBE0} = (1 - \alpha)E_x^{PBE} + \alpha E_x^{HF} + E_c^{PBE}, \quad (5.4)$$

where α is the mixing parameter to decide the balance between the exchange energy, denoted x of Hartree-Fock with PBE. Alike the last term represent the correlation energy from the PBE functional. This parameter alpha is determined empirically, thus making hybrid functional a semi-empirical model. Obviously considering the exact exchange in Hartree-Fock is a computationally challenging prospect. Heyd-Scuseria-Ernzerhof managed to lower the cost by the concept of Screened functionals that separate the Coloumb interaction into long-range and short-range interaction by a function $erfc(\mu r)$. These are known as HSE functionals [12], one of the superior methods for accurate band gaps is the HSE06 hybrid functional [13], with $\alpha = 0.25$ and $\mu = 0.11$.

5.1.5 Outlook

In many cases LDA and GGA suffice, PBE especially is by most considered the conventional standard for DFT calculations, for its balance of accuracy, cost and wide range applicability. However, distinctly concerning the band gap of a solids, both of these fall short. This is because the band gap of DFT calculations is complicated by the fact that the derivative of the XC-functional is discontinues with respect to the electron concentration [14], thus the simpler functionals fail to recall the experimental values since the total band gap in DFT is the fundamental gap (valence - conduction) + this contribution. This is corrected in meta-GGA and hybrid functionals

in the generalized Kohn-Sham scheme. Lastly, we would like to refer the reader to the work of Borlido, Aull, Huran, Tran, Marques, and Botti whom in 2019 conducted an exhaustive investigation of the band gap of over 470 unique non-magnetic compounds in order to benchmark the relative performance of several of the available and wideley used XC-functionals [10]. In this large-scale project they found overwhelming confirmation that the HSE06 functional followed closely by Modified-Becke Johnson is the superior choice for accurate band-gap measures. Regarding the SCAN functional, in several cases this yielded outputs very comparable to MBJ, and produce much better formation energies than PBE, but tends to overestimate in magnetic alloys. On the other side both LDA and PBE resulted in 50% and 30% under-estimation of the band gap or in several cases miss-classified compounds as metals, this was particularly evident in materials containing Ni and other 3d elements.

5.2 Practical aspects

The single-electron wavefunction have an analytic solution for a free electron $\psi_k = Ae^{ikr}$. In a crystalline matter with a periodic potential $V(\mathbf{r}) = V(\mathbf{r} + \mathbf{R})$, the single-electron wavefunction takes the form

$$\psi_k(\mathbf{r}) = u_k(\mathbf{r})e^{i\mathbf{k}\cdot\mathbf{r}}, \quad (5.5)$$

where $u_k(\mathbf{r})$ is a Bloch wave with the periodicity of the crystal and $e^{i\mathbf{k}\cdot\mathbf{r}}$ is called a plane wave. Because we use plane waves, DFT calculations are often referred to as plane wave calculations. The Bloch wave is the sum of all plane waves with wave vector equal to the reciprocal wave vector \mathbf{G} , described as

$$u_k(\mathbf{r}) = \sum_{\mathbf{G}} u_{k+\mathbf{G}} e^{i\mathbf{G}\cdot\mathbf{r}}, \quad (5.6)$$

which gives us the final expression for $\psi_k(\mathbf{r})$

$$\psi_k(\mathbf{r}) = \sum_{\mathbf{G}} c_{k+\mathbf{G}} e^{i(\mathbf{k}+\mathbf{G})\cdot\mathbf{r}} \quad (5.7)$$

The consequence from this expression is that evaluating the wavefunction of an electron at a single k point demand a summation over the entirety of reciprocal space. In order to reduce this computational burden, we can introduce a maximum cutoff value of the energy E_{cut} . This is possible because equation .. is the solution of the Shrödinger equation with kinetic energy

$$E = \frac{\hbar^2}{2m} |\mathbf{k} + \mathbf{G}|^2. \quad (5.8)$$

Seeing as the solution with lower energies are the most interesting, we can limit the calculations to plane waves with energy less than E_{cut} as

$$E_{\text{cut}} = \frac{\hbar^2}{2m} G_{\text{cut}}^2. \quad (5.9)$$

Thus, we can reduce the infinitely large sum above to a much more feasible calculation

$$\psi_{\mathbf{k}}(\mathbf{r}) = \sum_{|\mathbf{k}+\mathbf{G}| < G_{\text{cut}}} u_{\mathbf{k}+\mathbf{G}}(\mathbf{r}) e^{i(\mathbf{k}+\mathbf{G})\mathbf{r}}. \quad (5.10)$$

The cutoff value can be found by performing a set of calculations with different value and observe the convergence with respect to the total energy of the system.

A central concept of DFT calculations is that they are carried out in \mathbf{k} -space, as seen in equation 5.5. An additional point as to why this is done is that a number of calculations in DFT revolve around solving integrals of the type

$$g = \frac{V_{\text{cell}}}{(2\pi)^3} \int_{\text{BZ}} g(\mathbf{k}) d\mathbf{k}, \quad (5.11)$$

such as the density of states. Note that "BZ" indicate that the integral is evaluated for all \mathbf{k} in the Brillouin zone. This integral can be approximated by evaluating it at a set of discrete \mathbf{k} -points in reciprocal space and summing over the points with appropriately assigned weights. A larger set of points leads to more exact approximations. The method for selecting \mathbf{k} -points in reciprocal space was developed by Monkhorst and Pack in 1976, where one specify a number of points in each dimension $N_x N_y N_z$. Recalling that reciprocal space is inverse to regular space, supercells with equal and large dimensions converge at smaller values of N , and inversly for cells of small dimsion. The total number of \mathbf{k} -points required for accurate can be reduced by utulizing the symmetry of the cell, in which we can exactly approximate the entire BZ by extending a lesser zone through symmetry of the crystal lattice. This reduced zone is named the irreducible Brillouin zone (IBZ).

Metals in particular require a large set of \mathbf{k} -points for accurate results. This is because we encounter discontinues integrals in the Brillouin zone around the fermi suface where the states discontinusly change from occupied to non-occupied. To reduce the cost of this operation, there are two primary methods, tetrhaedon and smearing. The idea behind the tetrahedon method is to use the discrete set of \mathbf{k} -points to fill the reciprocal space with tethraeda and interpolate the function within each tethraeda such that the function can be integrated in the entire space rather than at discrete points. The latter approach for solving discontinuos integrals is to smear out the discontinuity and thus transforming the integral to a continuous one. A good analogy to this method is the fermi-dirac function, in which a small variable σ transform a step-function into a continuous function that can be integrated by standard methods.

A final consideration to how DFT is applied in practice is how the core electrons are handled. Tightly bound core electrons as opposed to valence electrons demand a greater number of plane-waves to converge. The most efficient method of reducing the expenses of core-electrons are so-called pseudopotentials. This method works by approximating the electron density of the core electrons by a constant density that mimic

the properties of true ion core and core electrons. This density is then remained constant for all subsequent calculations, ie only considering the valence electrons while regarding the core electrons as frozen-in. There are currently two popular types of pseudopotentials used in DFT, so-called ultrasoft pseudopotentials (USPPs) developed by Vanderbilt, and the projector augmented-wave (PAW) method by Bloch [15], [16].

5.3 Self-consistent field calculation

Preluding this section, we have considered the fundamental theory of DFT and it's practical ability to model various materials. Figure 5.2 illustrate the self-consistent field calculation scheme for how DFT calculations are performed in practice. The initial problem posed by DFT is that all properties rely on the density, and are dependent on each other. For instance, the effective potential is dependent on the density, which again is dependent on the eigenfunctions, that rely on the effective potential again. The cleaver approach begin with an initial guess to the density from which we can solve the Kohn-Sham equation and obtain the corresponding eigenfunctions. Following is an iterative method where we apply the recently calculated eigenfunctions to determine a new density and repeat the procedure above. This is repeated until the total energy is converged, by an own-defined criterion. Equivalently, the optimal ionic positions can be found by a similar approach. This method is based on quasi-Newton algorithms to minimize the forces between ions.

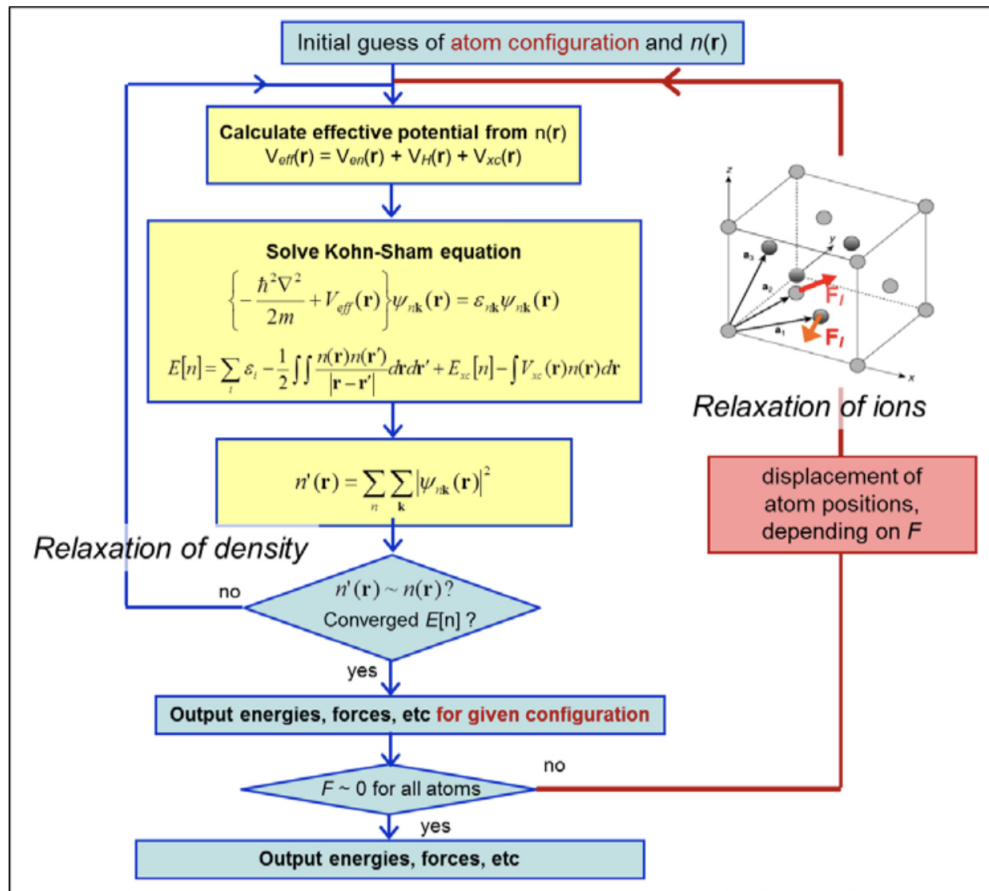


Figure 5.2: Self consistent iteration of a DFT calculation. Figure adopted from lecture notes [fys-mena4111](#) cite

Part III

Results and Discussion

Part IV

Conclusion

Write conclusion here

Bibliography

- [1] John P Perdew and Yue Wang. ‘Accurate and simple analytic representation of the electron-gas correlation energy’. In: *Physical review B* 45.23 (1992), p. 13244.
- [2] John P Perdew, Kieron Burke and Matthias Ernzerhof. ‘Generalized gradient approximation made simple’. In: *Physical review letters* 77.18 (1996), p. 3865.
- [3] Fabian (<https://mattermodeling.stackexchange.com/users/295/fabian>). *What makes PBE the most preferred functional over other GGA functionals?* Matter Modeling Stack Exchange. URL: <https://mattermodeling.stackexchange.com/q/402>.
- [4] Jianmin Tao et al. ‘Climbing the Density Functional Ladder: Nonempirical Meta-Generalized Gradient Approximation Designed for Molecules and Solids’. In: *Phys. Rev. Lett.* 91 (14 Sept. 2003), p. 146401. DOI: 10.1103/PhysRevLett.91.146401. URL: <https://link.aps.org/doi/10.1103/PhysRevLett.91.146401>.
- [5] Fabien Tran and Peter Blaha. ‘Importance of the Kinetic Energy Density for Band Gap Calculations in Solids with Density Functional Theory’. In: *The Journal of Physical Chemistry A* 121.17 (2017). PMID: 28402113, pp. 3318–3325. DOI: 10.1021/acs.jpca.7b02882. eprint: <https://doi.org/10.1021/acs.jpca.7b02882>. URL: <https://doi.org/10.1021/acs.jpca.7b02882>.
- [6] Jianwei Sun, Adrienn Ruzsinszky and John P. Perdew. ‘Strongly Constrained and Appropriately Normed Semilocal Density Functional’. In: *Phys. Rev. Lett.* 115 (3 July 2015), p. 036402. DOI: 10.1103/PhysRevLett.115.036402. URL: <https://link.aps.org/doi/10.1103/PhysRevLett.115.036402>.
- [7] Jianwei Sun et al. ‘Accurate first-principles structures and energies of diversely bonded systems from an efficient density functional’. In: *Nature chemistry* 8.9 (2016), pp. 831–836.
- [8] Arup Chakraborty et al. ‘Predicting accurate cathode properties of layered oxide materials using the SCAN meta-GGA density functional’. In: *npj Computational Materials* 4.1 (2018), pp. 1–9.
- [9] Axel D Becke and Erin R Johnson. ‘A simple effective potential for exchange’. In: *The Journal of chemical physics* 124.22 (2006), p. 221101.

- [10] Pedro Borlido et al. 'Large-Scale Benchmark of Exchange–Correlation Functionals for the Determination of Electronic Band Gaps of Solids'. In: *Journal of Chemical Theory and Computation* 15.9 (2019). PMID: 31306006, pp. 5069–5079. DOI: 10.1021/acs.jctc.9b00322. eprint: <https://doi.org/10.1021/acs.jctc.9b00322>. URL: <https://doi.org/10.1021/acs.jctc.9b00322>.
- [11] Carlo Adamo and Vincenzo Barone. 'Toward reliable density functional methods without adjustable parameters: The PBE0 model'. In: *The Journal of Chemical Physics* 110.13 (1999), pp. 6158–6170. DOI: 10.1063/1.478522. eprint: <https://doi.org/10.1063/1.478522>. URL: <https://doi.org/10.1063/1.478522>.
- [12] Aliaksandr V. Krukau et al. 'Influence of the exchange screening parameter on the performance of screened hybrid functionals'. In: *The Journal of Chemical Physics* 125.22 (2006), p. 224106. DOI: 10.1063/1.2404663. eprint: <https://doi.org/10.1063/1.2404663>. URL: <https://doi.org/10.1063/1.2404663>.
- [13] Jochen Heyd, Gustavo E Scuseria and Matthias Ernzerhof. 'Hybrid functionals based on a screened Coulomb potential'. In: *The Journal of chemical physics* 118.18 (2003), pp. 8207–8215.
- [14] Paula Mori-Sánchez and Aron J. Cohen. 'The derivative discontinuity of the exchange–correlation functional'. In: *Phys. Chem. Chem. Phys.* 16 (28 2014), pp. 14378–14387. DOI: 10.1039/C4CP01170H. URL: <http://dx.doi.org/10.1039/C4CP01170H>.
- [15] G. Kresse and D. Joubert. 'From ultrasoft pseudopotentials to the projector augmented-wave method'. In: *Phys. Rev. B* 59 (3 Jan. 1999), pp. 1758–1775. DOI: 10.1103/PhysRevB.59.1758. URL: <https://link.aps.org/doi/10.1103/PhysRevB.59.1758>.
- [16] P. E. Blöchl. 'Projector augmented-wave method'. In: *Phys. Rev. B* 50 (24 Dec. 1994), pp. 17953–17979. DOI: 10.1103/PhysRevB.50.17953. URL: <https://link.aps.org/doi/10.1103/PhysRevB.50.17953>.